1. Section SA

In the present section, parameters α_0, n, ε, ϕ characterizing the erosion behavior of EB-PVD TC are determined through the method described in [1] using experimentally measured erosion rates at different temperatures [2,3], (Table S1).

Table S1. The experimentally measured erosion rate of EB-PVD TBCs [2,3].

Temperature (°C)	Impact Velocity(m/s)	Erodent	Impact Angles (°)	Erosion Rates (g/kg)
Room Temperature (RT)	170	60 μm SiO₂	30	9.58
			60	15.44
			75	17.39
			90	18.3
540 °C	122	40 μm Al₂O₃	15	2.06
			20	3.98
			25	5.09
			36	7.62
			53	10.76
			83	14.33
			90	14.7
910 °C	300	60 μm SiO₂	30	27
			45	25.2
			60	16.7
			75	8.9
			90	5.4

1.1. Erosion Curves and Parameters Characterizing the Erosion Behavior of EB-PVD TC at RT and 540 °C

Typically, a brittle erosion is found according to erosion data measured for EB-PVD TC with silica erodent at RT and with alumina erodent at 540°C, where the maximum erosion rate is identified at an impact angle of 90°. The procedure to estimate the parameters characterizing the erosion behavior of brittle material is used and described in following steps.

(1) Considering the negligible critical impact velocity K for brittle material (see Section 3.3), the deformation wear kinetic energy ε can be estimated using Equation (S1) with the experimentally measured erosion rate at 90° W_t, the accumulated impact mass M and impact velocity V from

$$\varepsilon = \frac{1}{2} MV^2 / W_t \big|_{\alpha=90^o} \qquad \text{(S1)}$$

(2) Once the ε is determined, the deformation wear $W_d(\alpha)$ can be estimated at different angles using Equation (S2). The corresponding cutting wear $W_t(\alpha)$ can be calculated by subtracting the deformation wear $W_d(\alpha)$ from experimentally measured total erosion rate $W_c(\alpha)$ using Equation (S3), as

$$W_d(\alpha) = \frac{\frac{1}{2} M (V \sin \alpha)^2}{\varepsilon} \qquad \text{(S2)}$$

$$W_c(\alpha) = W_t(\alpha) - W_d(\alpha) \qquad \text{(S3)}$$

(3) The maximum cutting wear can therefore be identified at the specific maximum angle of cutting wear α_{cmax}, from which the erosion parameter n can be estimated by solving Equation (S4). The critical angle α_0 is calculated by substituting n into Equation (S2).

$$\sin n\alpha_{c\max} - \frac{n}{2}\frac{\cos n\alpha_{c\max}}{\tan n\alpha_{c\max}} = 0 \tag{S4}$$

(4) For brittle erosion, there is no "turning point" at which the maximum erosion rate is found at a specific impact angle. According to [1], the cutting wear kinetic energy ϕ is evaluated based on the comparison between the angle giving half of the erosion experienced at 90° ($\alpha_{1/2}$)and the critical angle α_0, as shown in Equation (S5).

$$\phi = \begin{cases} \varepsilon \times \left(\dfrac{\cos^2 \alpha_{\frac{1}{2}}}{\dfrac{1}{2} - \sin^2 \alpha_{\frac{1}{2}}} \right) & \alpha_{\frac{1}{2}} > \alpha_0 \\[4mm] \varepsilon \times \left(\dfrac{\cos^2 \alpha_{\frac{1}{2}} \sin n\alpha_{\frac{1}{2}}}{\dfrac{1}{2} - \sin^2 \alpha_{\frac{1}{2}}} \right) & \alpha_{\frac{1}{2}} < \alpha_0 \end{cases} \tag{S5}$$

Substituting the experimentally measured erosion rates at RT and 540 °C into Equations (S1)–(S5), parameters characterizing the erosion behavior of EB-PVD TC are identified and tabulated in Table S2. The erosion rates are calculated as a function of impact angles and illustrated in Figures S1 and S2 together with experimentally measured erosion rates.
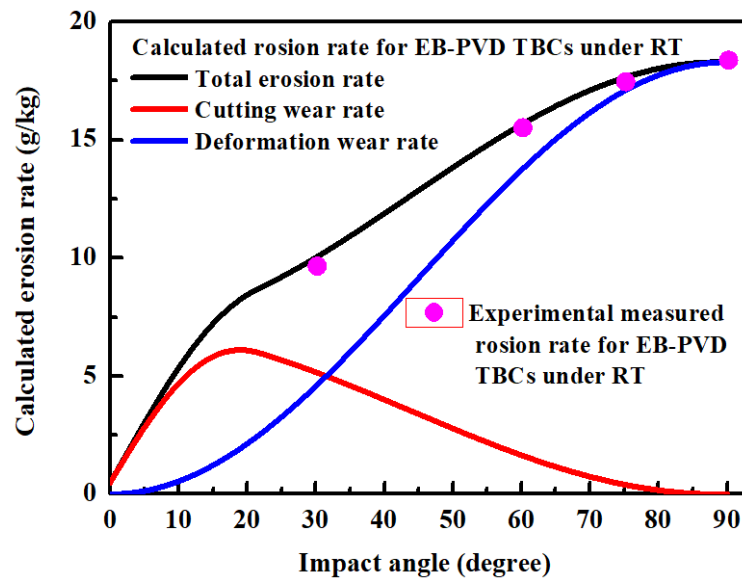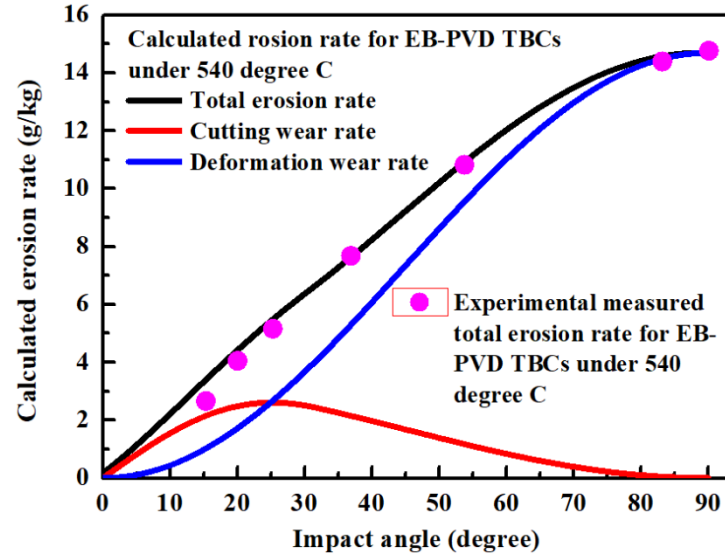

**Figure S1.** The calculated erosion rate of EB-PVD TC under impact of silica particles at RT.

Figure S2. The calculated erosion rate of EB-PVD TC under impact of alumina particles at 540 ℃.

1.2. Parameters Characterizing the Erosion Behavior of EB-PVD TC at 910 ℃ and Erosion Curve

Ductile erosion is found for EB-PVD TC erosion data with silica erodent at 910 ℃, where the maximum erosion rate (estimated at turning point) is identified at an impact angle of $\alpha_{max} = 30^0$. The method to evaluate the parameters characterizing the erosion behavior are identical to steps (1)–(3) in Section 1.1, except for the cutting wear kinetic energy ϕ, which is estimated by

$$\phi = \varepsilon \times \left(\sin n\alpha_{max} - \frac{n}{2} \frac{\cos n\alpha_{max}}{\tan n\alpha_{max}} \right) \tag{S6}$$

However, due to the limited experimental data (none of the erosion data are provided for $\alpha < \alpha_{max}$), it is impossible to identify the maximum angle of cutting wear α_{max} following the regular sequence of steps from (1)–(4). In the present study, assuming measured erosion data fall into the range $\alpha > \alpha_o$, cutting wear kinetic energy ϕ is obtained by fitting measured total erosion rates into expression 1B in Equation (1), with deformation wear kinetic energy ε estimated from steps (1)–(2) in Section 1.1 (Figure S3).
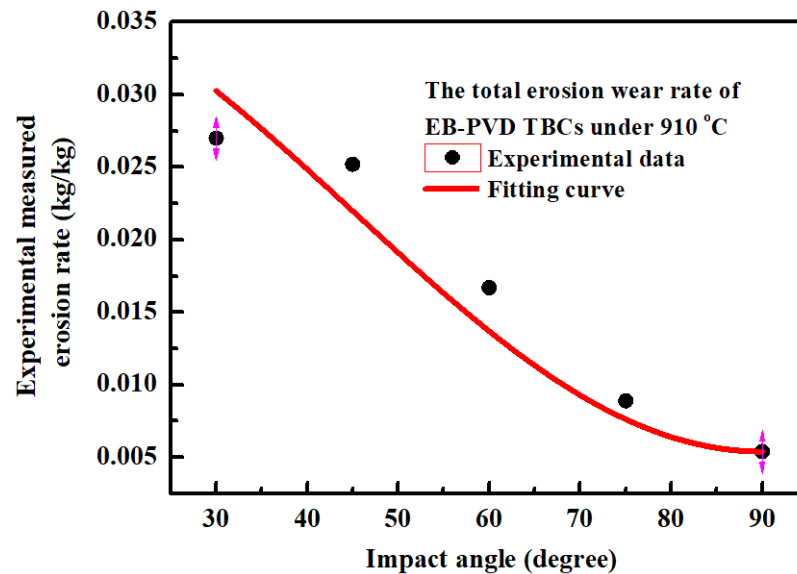
Figure S3. The experimentally measured erosion rates at 910 °C with fitting curve used to obtain the cutting wear kinetic energy ϕ.

Therefore, the parameter n is obtained by substituting ϕ and solving Equation (S6), where α_o is estimated by Equation (2). The maximum angle of cutting wear can be estimated by substituting n into Equation (S4) ($\alpha_{max} \approx = 28.82^0$ for erosion curve at 910°C). Parameters characterizing the erosion behavior of EB-PVD TC at 910 °C are tabulated in Table S2. The erosion rates are calculated as a function of impact angles and illustrated in Figure S 4, together with experimentally measured erosion rates.
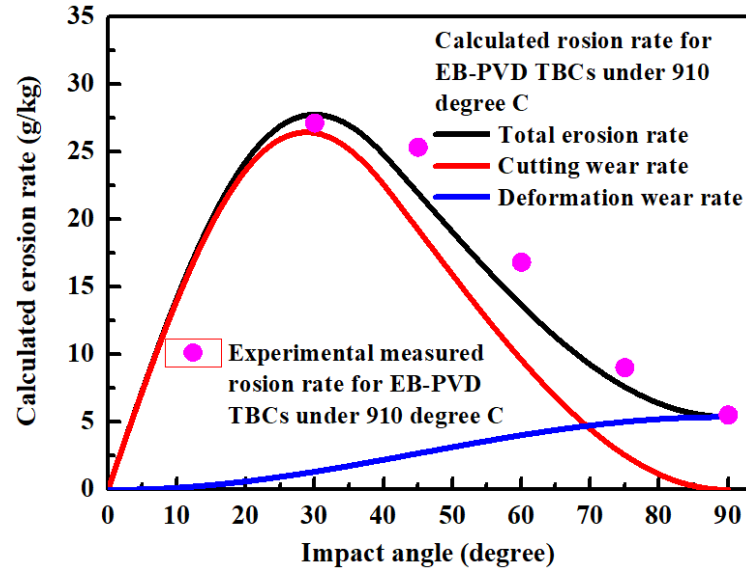

Figure S4. The calculated erosion rate of EB-PVD TC under impact of silica particles at 910 °C.

Table S2. Parameters characterizing the erosion behavior of EB-PVD TC at different temperatures.

Temperatures (°C)	Impact Velocity (m/s)	Erodent	Cutting Wear Kinetic Energy ϕ (m^2/s^2)	Deformation Wear Kinetic Energy ε (m^2/s^2)	n	α_0 (°)
20	170	60 µm SiO$_2$	2.05×10^6	7.90×10^5	3.982	22.60
540	122	40 µm Al$_2$O$_3$	2.21×10^6	5.06×10^5	2.841	31.698
910	300	60 µm SiO$_2$	1.17×10^6	8.33×10^6	2.202	40.87

2. Section SB

In the present section, the effect of critical velocity on the deformation wear kinetic energy is evaluated. The critical impact velocity K is evaluated by substituting the temperature-dependent yield strength and the out-of-plane elastic modulus into Equation (8), and the results are illustrated in Figure S5.
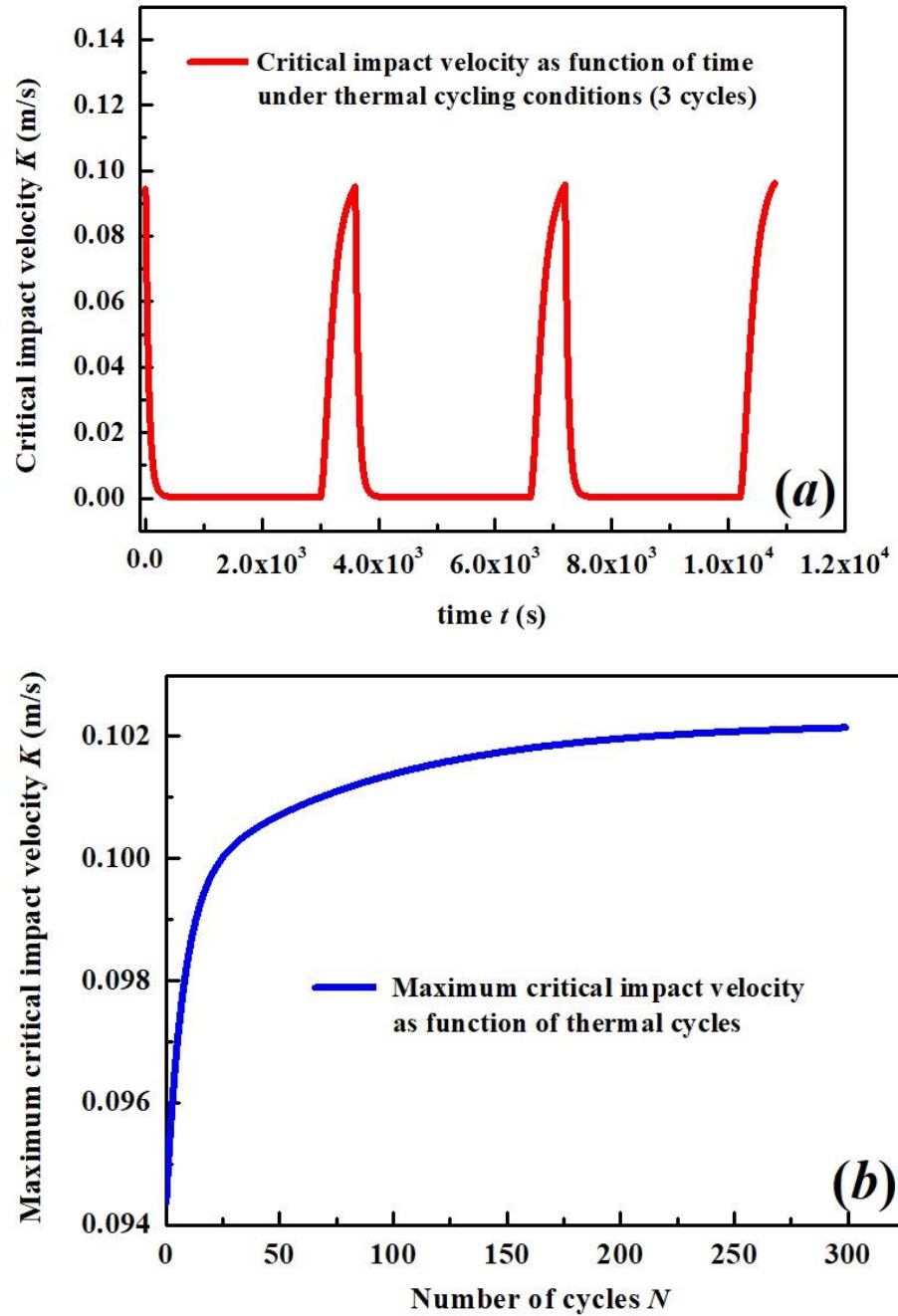
Figure S5. The calculated critical impact velocity of EB-PVD TC (**a**) as a function of time for three cycles (**b**) as a function of number of cycles.

It is evident that the value of critical impact velocity is much less than the impact velocity applied at either RT (170 m/s) or 910 °C (300 m/s). This indicates that the contribution of deformation wear generated from vertical impact of erodent cannot be neglected throughout the thermal cycles. For simplification, the critical impact velocity is neglected from the analytical expression of deformation wear kinetic energy in Equation (13).

In the present section, the effect of sintering of TC on the kinetic energies are evaluated. Hutchinson et al. [4] proposed an analytical model to evaluate the energy release rate generated due to the sintering cracks, as the top surface of coating is at a sufficiently high temperature. The sintering cracks propagate perpendicular to the surface of the TC (within columns) initially. The cracks could reorient into a delamination at depth a when the sintering stress σ_s, developed over a depth H, is sufficiently large. The schematic

diagram of development of sintering cracks is illustrated in Figure S6. The expression of sintering crack energy release rate G_{Sint} is given by [4]

$$G_{sint} = \frac{4}{\pi}\left(\frac{\sigma_s^2 H}{\bar{E}_{TC}}\right)\left(\frac{a}{H}\right)\left[\left(1.3 - 0.18\frac{H}{a}\right)\sin^{-1}\left(\frac{H}{a}\right)\right]^2 \qquad (S7)$$

where $\bar{E}_{TC}$ is the TC effective elastic modulus. In Equation (S7), a defines the depth of the crack developing from the surface of the TC to the position where the crack reorients into a delamination crack that propagates laterally. In other words, the length of sintering cracks determines the position of potential damage which may be exerted by the external erosion process.
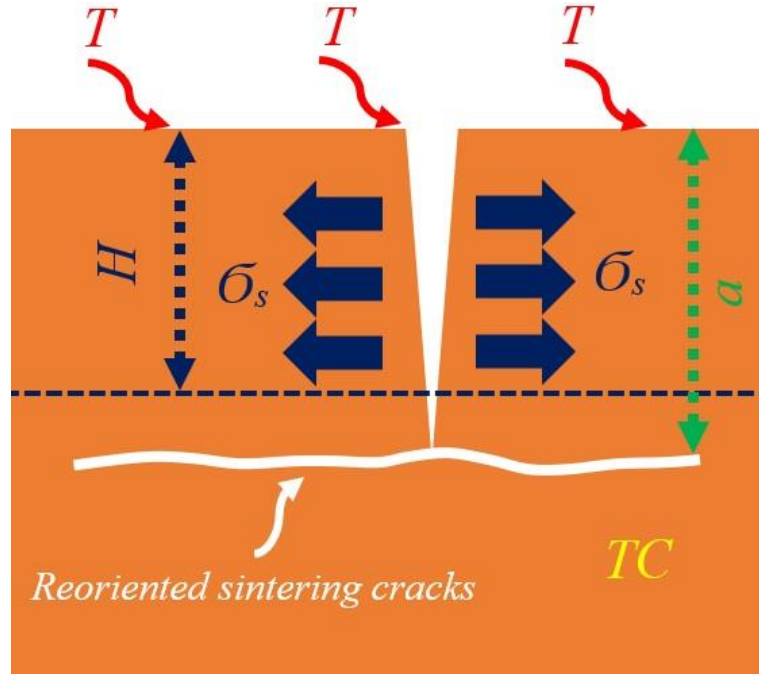
Figure S6. The schematic diagram of sintering crack developed within TC [4].

The cutting wear and deformation wear kinetic energy indicate the erosion resistance of the TC layer. Therefore, it is assumed that temperature- and time-dependent behavior can be described by incorporating a function inversely proportional to sintering crack length generated during high-temperature dwell time, as shown in Equation (30).

The abovementioned parameter H in Equation (S7) indicates the depth of sintering stress generated within the TC layer. In the present study, the value of H is assumed to be the maximum depth of penetration Z_{max} that is able to be reached and eroded for spherical particles, shown in Equation (9). The sintering stress is given by [5],

$$\sigma_s = \frac{2\gamma}{r_p} \qquad (S8)$$

Where γ is the surface free energy per unit area given by [6],

$$\gamma = 1.927 - 0.428 \times 10^3 T \qquad (S9)$$

γ is a constant during sintering crack growth and high-temperature dwell time. γ_p in Equation (S8) is the mean pore radius given by [5],

$$r_p = \frac{\left[(1-\rho_{rl})/6\right]^{1/3} L}{2} \tag{S10}$$

L is the average size of isotropic grains composing YSZ columns and given by [7],

$$\dot{L} = \dot{L}_0 \exp\left(-\frac{Q}{RT}\right)\left(\frac{L_0}{L}\right)^{\beta-1}(1-\rho_i)^{-\frac{\beta-1}{2}} \tag{S11}$$

where $\dot{L}_0 = 2 \times 10^{-3}\ \mu m/s$, Q=192 kJ/mol, R=8.314 and β =5 [7]. The average grain size L as a function of time can be solved by a fourth-order Runge–Kutta method. It is assumed that the propagation of cracks within the TC occurs as the energy release rate reaches the critical through-thickness fracture toughness, given in [8] and modified into Equation (S12) as

$$G_{sint} = \left\{\alpha - \beta\left[1-\exp\left(\gamma\frac{a}{Z_{max}}\right)\right]^2\right\}G_{crit}^0 \tag{S12}$$

Here, the value of fitting parameters α=1, β=0.9 and γ=0.693 are determined by the assumption in [8] as

$$\begin{cases} G_{sint} = G_{crit}^0 & for\ \ a = 0 \\ G_{sint} = 0.1 G_{crit}^0 & for\ \ a \to \infty \end{cases} \tag{S13}$$

G_{crit}^0 is the theoretical through-thickness toughness of the TC and is given by 1J/m² [9]. The calculated critical through-thickness fracture toughness is illustrated in Figure S7 as a function of crack length a.
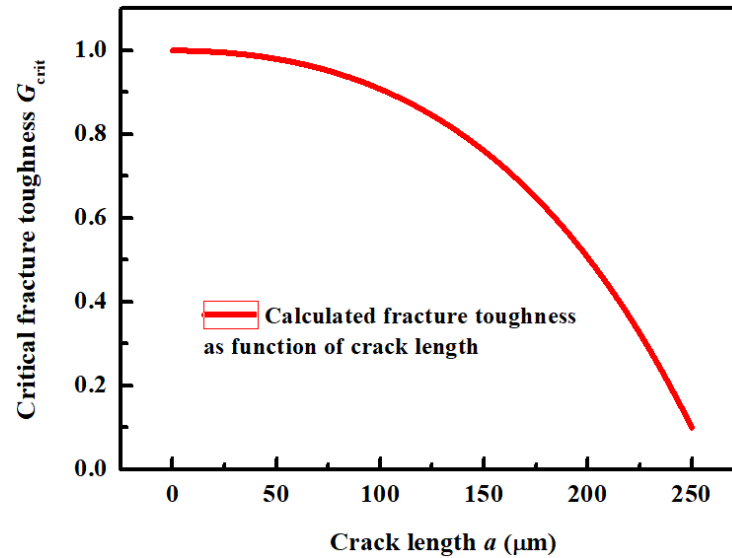
Figure S7. Calculated critical through-thickness fracture toughness as function of crack length.

The Equation (S7) can be rewritten as Equation (S14) in order to use the fourth-order Runge–Kutta method to derive the correlation between sintering crack length a to high-temperature dwell time t_{HIGH} as

$$F(t,a) = G_{sint} - \frac{4}{\pi}\left(\frac{\sigma_s^2 Z_{max}}{\bar{E}_{TC}}\right)\left(\frac{a}{Z_{max}}\right)\left[\left(1.3 - 0.18\frac{Z_{max}}{a}\right)\sin^{-1}\left(\frac{Z_{max}}{a}\right)\right]^2 \tag{S14}$$

where

$$\frac{da}{dt} = -\frac{F_t(t,a)}{F_a(t,a)} \tag{S15}$$

The sintering crack length a is obtained by integrating Equation (S15) with respect to time, and the results are illustrated in Figure S8 as a function of high-temperature dwell time t_{HIGH}.
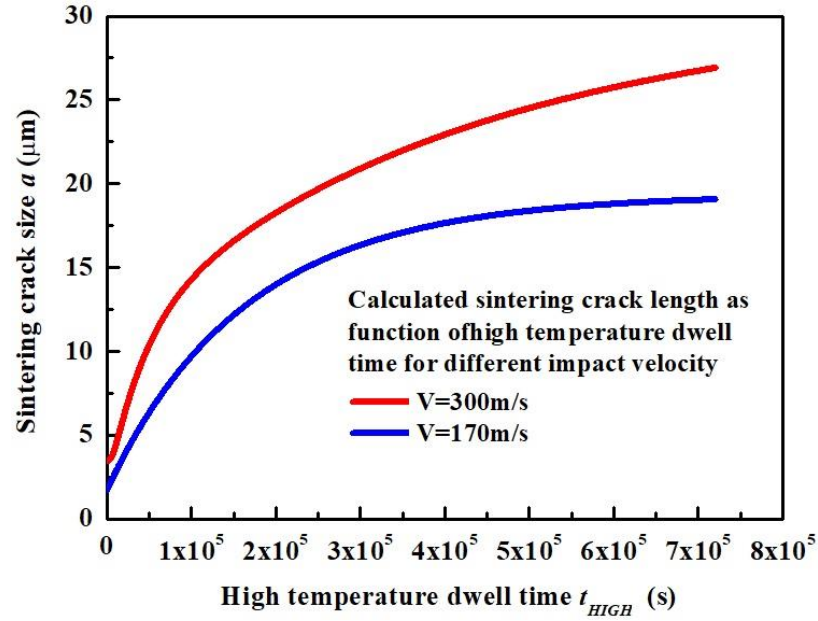
Figure S8. Sintering crack length as function of high-temperature dwell time.

The calculated crack length in Figure S8 indicates the depth that the sintering crack reaches and the position of the plane where the crack reorientation occurs. It is evident that the crack length increases rapidly at the beginning of dwell time. This can be explained by the significant sintering effect at the early stage of high-temperature dwell time, where elevated temperatures at the surface of the TC lead to a high magnitude of sintering crack. This is the driving force that initiates the vertical crack propagation and reorientation at a given crack length a. The crack growth rate decreases at the later stage of high-temperature dwell time. This corresponds to a decrease of sintering stress (r_p increase in Equation (S8) results in a decrease in σ_S in Equation (S7)), and an increase in elastic modulus equation $\bar{E}_{TC}$ in Equation (S7), which generally lowers the sintering crack driving force. This may also indicate that at later dwell time, the erosion rates are higher where the sintering cracks reorient. However, the erosion rate decreases as a function of sintering time.

3. Section SC

In the present section, the validation of the temperature-process-dependent erosion model is described. The calculated results are illustrated and compared with erosion rates measured experimentally. The model parameters η'' and ξ' in Equation (27) and Equation (28) are fitted using the erosion rate measured experimentally at RT and 910°C, with impact velocity 170 m/s and 300 m/s, respectively. The sintering parameters $f(a)$ and $g(a)$ in Equation (30) are fitted using erosion rates measured experimentally with different sintering temperatures and time [10,11].

*3.1. Validation of Temperature-Dependent Erosion Behavior*

To calibrate the temperature-dependent model parameters $\eta''(T)$ and $\xi''(T)$ in Equation (27) and Equation (28), the erosion rate is calculated with Equation (1) at the first cycle to minimize the effect of time-dependent sintering behavior on the estimated cutting wear and deformation wear kinetic energy. The temperature is selected ranging from RT to 1400 °C, where erodent parameters, including impact angles, impact mass and impact velocity (170,300 m/s), are tabulated in Table S3, based on experimentally measured erosion rates [12].

Table S3. Parameters used to calculate temperature-dependent fitting parameters.

| # of Cycle	Temperatures (°C)	Impact Angles (°)	Impact Mass (kg)	Impact Velocity (m/s)
Determined cycle number N: 1	Determined T ranging from [RT, 1400]	Determined α ranging from [5-90]	Determined accumulated mass M=1	Determined V: 170,300

Figure S9 illustrates the calculated erosion rates at the first thermal cycle for different temperatures. Figure S9(a) shows erosion rates measured experimentally at RT with impact velocity 170 m/s, and Figure S9 (b) shows erosion rates at 910 °C with impact velocity 300 m/s. Figure S9 indicates that the erosion rate decreases as temperature increases for silica particle–EB-PVD TC erosion system, i.e., there exists a significant drop in erosion rate at large angles as temperature increases. This in turn corresponds to an increase in deformation wear kinetic energy at elevated temperatures. The decrease in erosion rate at elevated temperatures is also experimentally measured in [13] for EB-PVD TC with silica particles. In addition, it is evident that apart from the erosion rates calculated at RT, the rest of the erosion curves indicate that the coating may be eroded in a pseudoductile manner at intermediate to elevated temperatures. This is related to the thermal property of silica erodent at elevated temperatures, which softens at about 500 °C [14]. The half-melted silica particles pull out the fractured columns at glancing angles, increasing the cutting wear, and are attached to fractured column at high angles. This decreases the deformation wear at elevated temperatures, leading to pseudoductile erosion curves calculated for most temperatures in Figure S9.
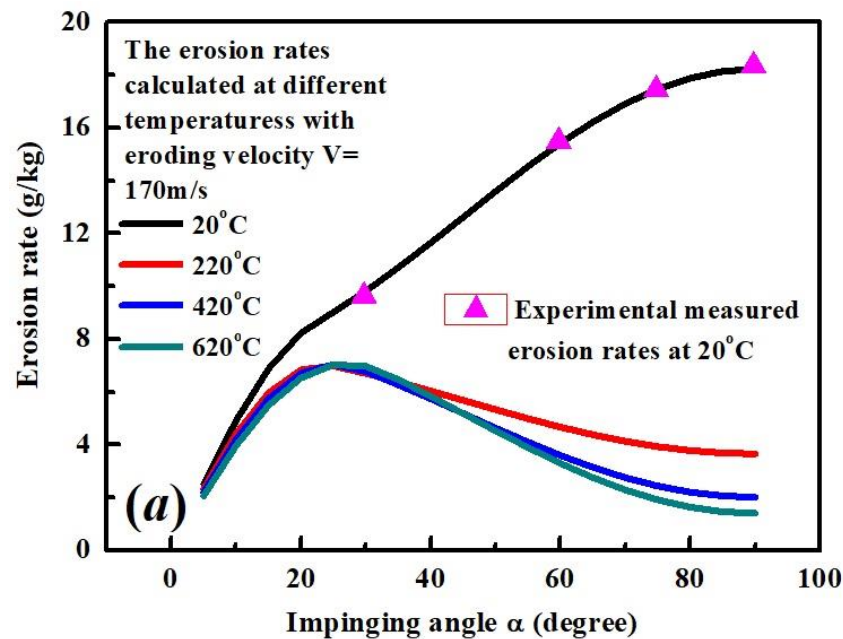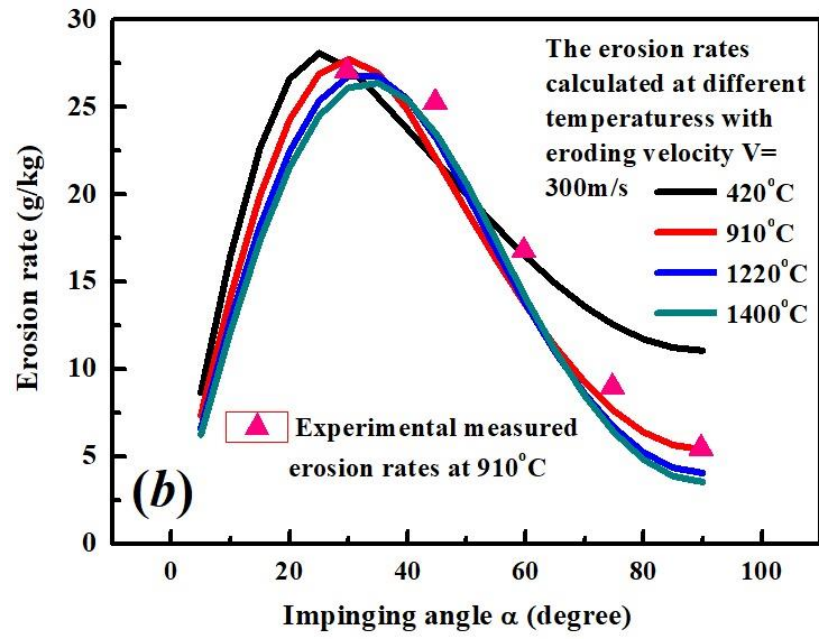
Figure S9. Calculated erosion rates as a function of impact angles at first thermal cycle for different temperatures with erosion rates measured experimentally [12] using (**a**) impact velocity 170 m/s (**b**) impact velocity 300 m/s.

In addition, the ratio of cutting wear (estimated by (A) and (C) in Equation (1)) to deformation wear (estimated by (B) in Equation (1)) is calculated and evaluated as a function of different impinging angles for various of temperatures, as shown in Figure S10.
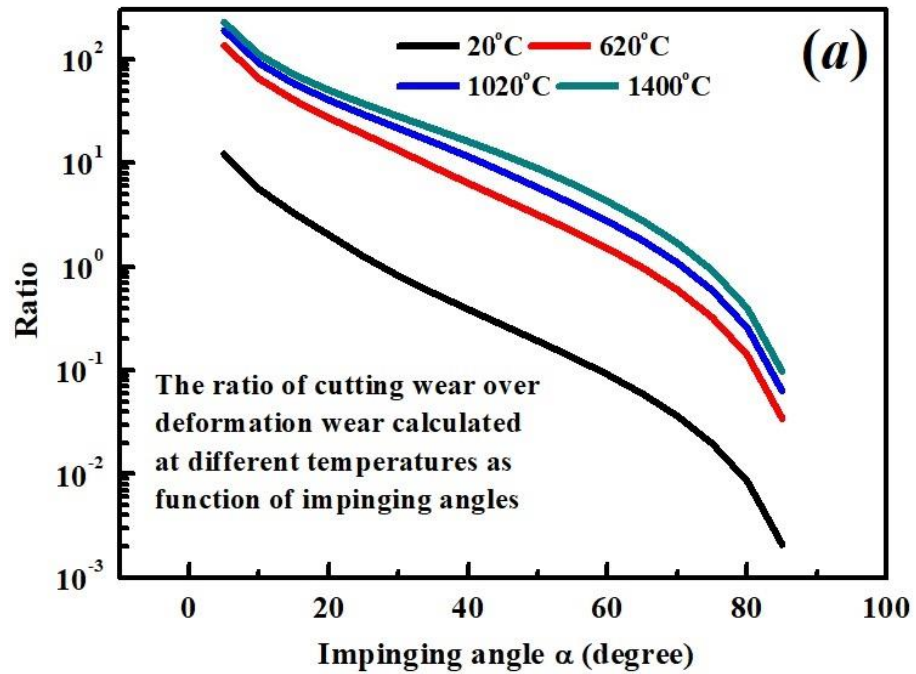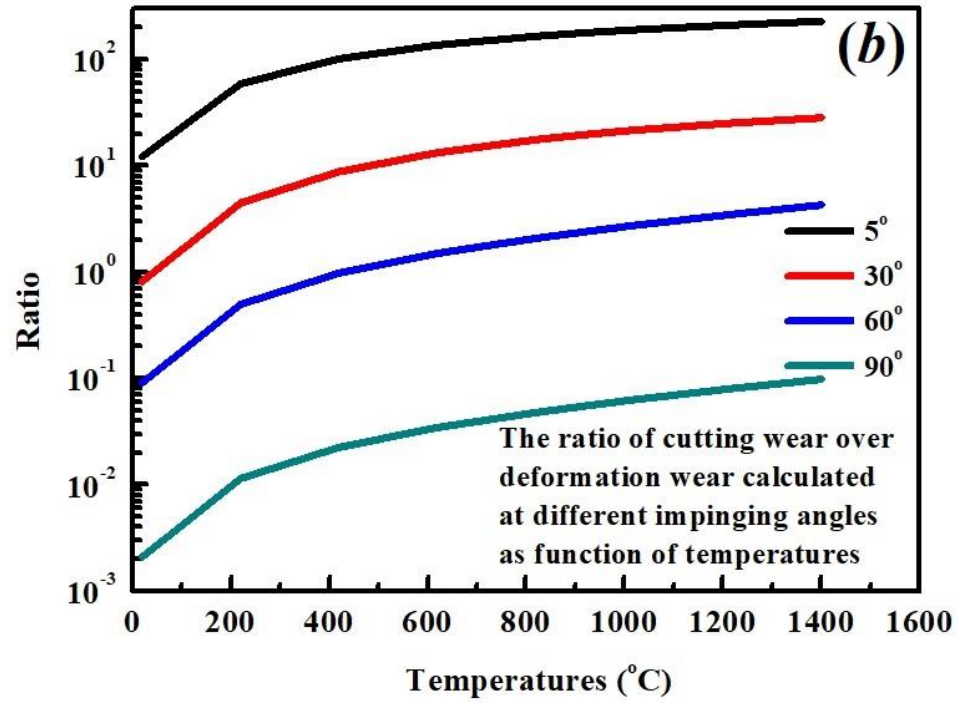
Figure S10. The calculated ratio of cutting wear over deformation wear as function of (**a**) different impinging angles and (**b**) various of temperatures.

It is evident that the ratio drops dramatically as the calculated impinging angles increase from 0 to 90°. This corresponds to the fact that the erosion is dominated by cutting wear at shallow angles with an increase in deformation wear as the impact angles increase, as shown in Figure S10(a). It should be noted that the ratio of cutting wear over deformation wear is higher at elevated temperatures compared to that at lower temperatures, as shown in Figure S10(b), especially for the ratio at shallow angles. The significant increase in cutting wear is explained by softening/partially melting/pasty of silica erodent that is capable of pulling out fractured sections of coating that otherwise cannot be removed at shallow angles [2,15,16].

3.2. Validation of Sintering Time-Dependent Erosion Behavior

To calibrate the $f(a)$ and $g(a)$ in Equation (30), erosion is calculated from Equation (15) based on erosion tests conducted for EB-PVD TC at three different sintering stages [10,11]. The details of the experimental preparations (including the TC presintering time and temperatures, parameters for erosion tests including impact angles, impact velocities and particle mass) are tabulated in Table S4. Note that the mass of erodent for individual particles described in [10,11] were determined by their size, ranging from 20 to 1000 μm. For the present work, the erosions are calculated using random parameter $m_i = \rho_p \times (4/3\pi R^3)$, where the radius R is assumed to vary randomly between 20 and 1000 μm.

Table S4. Parameters of experimental settings in [11] used to calculate sintering-dependent fitting parameters.

TC Presintering Time (h)	TC Presintering Temperatures (°C)	Particle Impact Angles (°)	Particle Impact Mass (kg)	Particle Impact Velocity (m/s)
0 (As received)	RT	Randomly selected α		Randomly selected V in
24	1500	ranging from		the range of [50, 400]

		[30, 90]	Randomly selected m_i
100	1100		where R is in the range
			of [20, 1000]

Figure S11 shows the calculated erosion rates for EB-PVD TC under various presintering treatments under different temperatures, together with experimentally measured erosion [10].
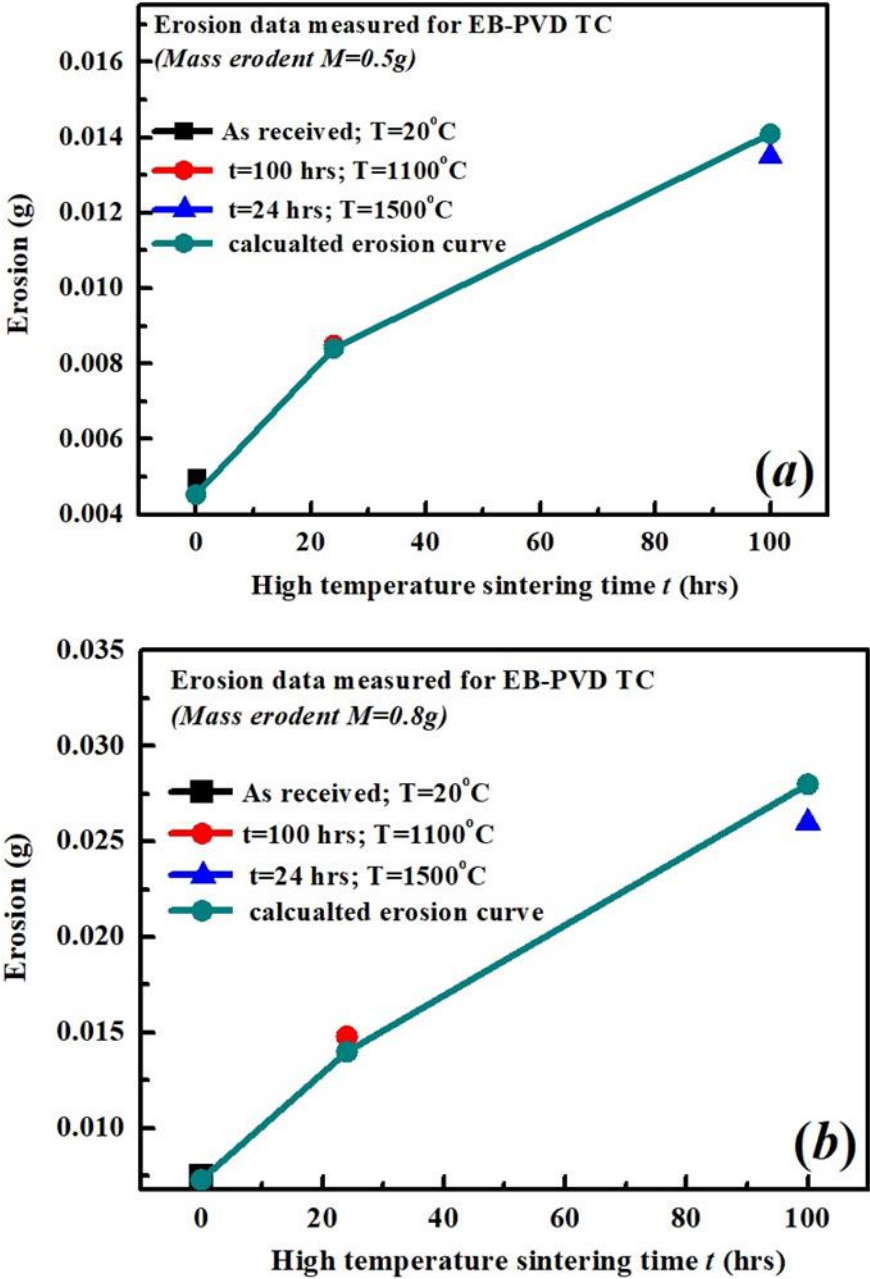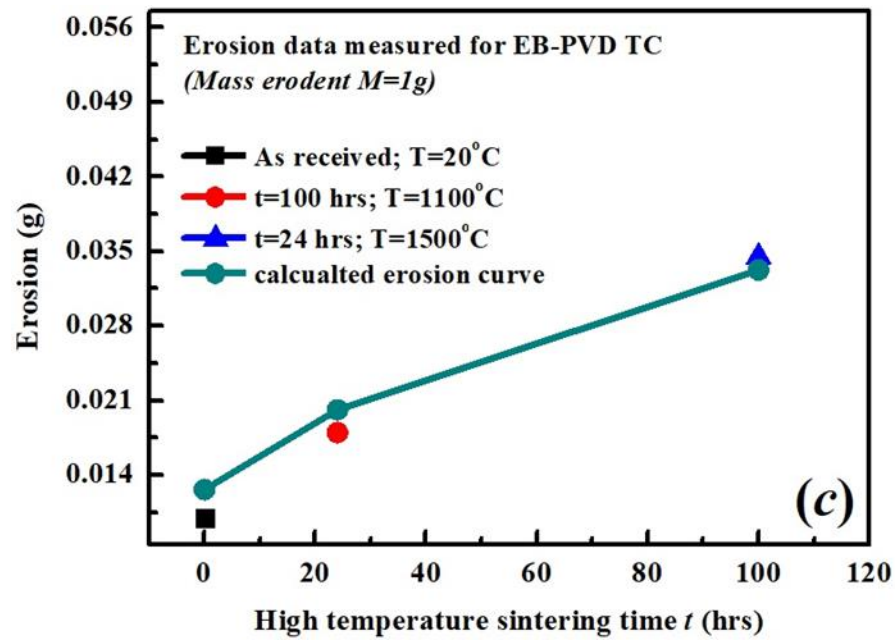
Figure S11. Calculated erosion as a function of high-temperature sintering time with erosion measured experimentally [10] for different accumulated mass (**a**) $M = 0.5$ g, (**b**) $M = 0.8$ g and (**c**) $M = 1$ g.

The fitting parameters in Equation (30) (calibrated from measured erosions in [11]) can be used to indicate the general trend of kinetic energies affected by sintering behavior of the TC. This follows since the erodent used in sintering erosion experiments is selected to be alumina particles with impact velocity in the range of 50–400 m/s. Instead, for the present study with the analytical model, the silica particles are selected with defined velocities ($V = 170$ and 300 m/s), which are then used to obtain the fitting parameters. In addition, unlike the procedure of estimating the temperature-dependent fitting parameters using deterministic functions, the sintering parameters are fitted by a stochastic approach described in Section 2.3, where the impact angles and mass during high-temperature dwell time are randomly selected.

References

[1]   J. H. Neilson and A. Gilchrist, "Erosion by a stream of solid particles," *Wear*, vol. 11, no. 2, pp. 111–122, Feb. 1968, doi: 10.1016/0043-1648(68)90591-7.

[2]   J. R. Nicholls, R. G. Wellman, and M. J. Deakin, "Erosion of thermal barrier coatings," *Mater. High Temp.*, vol. 20, no. 2, pp. 207–218, Jan. 2003, doi: 10.1179/mht.2003.024.

[3]   W. Tabakoff, "Investigation of coatings at high temperature for use in turbomachinery," *Surf. Coat. Technol.*, vol. 39–40, pp. 97–115, Dec. 1989, doi: 10.1016/0257-8972(89)90045-5.

[4]   J. W. Hutchinson and A. G. Evans, "On the delamination of thermal barrier coatings in a thermal gradient," *Surf. Coat. Technol.*, vol. 149, no. 2, pp. 179–184, Jan. 2002, doi: 10.1016/S0257-8972(01)01451-7.

[5]   Z.-Z. Du and A. C. F. Cocks, "Constitutive models for the sintering of ceramic components—I. Material models," *Acta Metall. Mater.*, vol. 40, no. 8, pp. 1969–1979, Aug. 1992, doi: 10.1016/0956-7151(92)90183-F.

[6]   A. Tsoga and P. Nikolopoulos, "Surface and grain-boundary energies in yttria-stabilized zirconia (YSZ-8 mol%)," *J. Mater. Sci.*, vol. 31, no. 20, pp. 5409–5413, Oct. 1996, doi: 10.1007/BF01159310.

[7]   E. P. Busso and Z. Q. Qian, "A mechanistic study of microcracking in transversely isotropic ceramic–metal systems," *Acta Mater.*, vol. 54, no. 2, pp. 325–338, Jan. 2006, doi: 10.1016/j.actamat.2005.09.003.

[8]   R. Vaßen, S. Giesen, and D. Stöver, "Lifetime of Plasma-Sprayed Thermal Barrier Coatings: Comparison of Numerical and Experimental Results," *J. Therm. Spray Technol.*, vol. 18, no. 5–6, p. 835, Sep. 2009, doi: 10.1007/s11666-009-9389-z.

[9]   B. Cheng *et al.*, "Sintering-induced delamination of thermal barrier coatings by gradient thermal cyclic test," *J. Am. Ceram. Soc.*, vol. 100, no. 5, pp. 1820–1830, 2017, doi: 10.1111/jace.14713.

[10]   R. G. Wellman, M. J. Deakin, and J. R. Nicholls, "The effect of TBC morphology and aging on the erosion rate of EB-PVD TBCs," *Tribol. Int.*, vol. 38, no. 9, pp. 798–804, Sep. 2005, doi: 10.1016/j.triboint.2005.02.008.

[11]   R. G. Wellman and J. R. Nicholls, "On the effect of ageing on the erosion of EB-PVD TBCs," *Surf. Coat. Technol.*, vol. 177–178, pp. 80–88, Jan. 2004, doi: 10.1016/j.surfcoat.2003.06.019.

[12]   J. R. Nicholls, Y. Jaslier, and D. S. Rickerby, "Erosion of EB-PVD thermal barrier coatings," *Mater. High Temp.*, vol. 15, no. 1, pp. 15–22, Jan. 1998, doi: 10.1080/09603409.1998.11689572.

[13]   S. Gokul Lakshmi, B. Malvi, D. S. Rao, D. K. Das, and M. Roy, "Comparison of erosion rate of EB-PVD and plasma sprayed TBC," *Surf. Eng.*, vol. 37, no. 11, pp. 1396–1403, Nov. 2021, doi: 10.1080/02670844.2021.1997251.

[14]   Goldsmith, A.; Hirschhorn, H.J.; Waterman, T.E. Ceramics. In *Handbook of Thermophysical Properties of Solid Materials*; Pergamon Press: Oxford, UK, 1961; Volume 3.

[15]   J. Chen, B. D. Beake, R. G. Wellman, J. R. Nicholls, and H. Dong, "An investigation into the correlation between nano-impact resistance and erosion performance of EB-PVD thermal barrier coatings on thermal ageing," *Surf. Coat. Technol.*, vol. 206, no. 23, pp. 4992–4998, Jul. 2012, doi: 10.1016/j.surfcoat.2012.06.011.

[16]   R. G. Wellman and J. R. Nicholls, "A Monte Carlo model for predicting the erosion rate of EB PVD TBCs," *Wear*, vol. 256, no. 9, pp. 889–899, May 2004, doi: 10.1016/j.wear.2003.09.001.